Terr. Atmos. Ocean. Sci., Vol. 27, No. 2, 303-309, April 2016 doi: 10.3319/TAO.2016.02.02.01(AA)

NOTES AND CORRESPONDENCE

Surface Air Temperature Evaluation from GPS Radio Occultation in Turbulent Heat Flux Estimation: Case Study in Tropical Oceans

Liang Chang[1, 2], Guoping Gao[1, 2, *], Lixin Guo[1, 2], Guiping Feng[1, 2], and Yang Zhang[1, 2]

[1] *Shanghai Ocean University, College of Marine Sciences, Shanghai, China*
[2] *Collaborative Innovation Center for Distant-Water Fisheries, College of Marine Sciences, Shanghai, China*

Received 1 October 2015, revised 25 November 2015, accepted 2 February 2016

ABSTRACT

Surface air temperature (SAT) retrieval at 2 m using Global Positioning System (GPS) radio occultation (RO) observations is presented in this paper. These measurements were further incorporated to estimate turbulent heat fluxes. The results show that the root mean square (RMS) of RO derived SAT (SAT_{RO}) is better than 1.1°C and the standard deviation (STD) is less than 0.9°C. Furthermore, the turbulent heat fluxes derived from RO observations show smaller deviations from the Tropical moored buoys than the other gridded products analyzed in this study, revealing that the SAT_{RO} is helpful in improving surface turbulent heat flux estimation.

Key words: GPS radio occultation, Surface air temperature, Turbulent heat flux

Citation: Chang, L., G. Gao, L. Guo, G. Feng, and Y. Zhang, 2016: Surface air temperature evaluation from GPS radio occultation in turbulent heat flux estimation: Case study in Tropical Oceans. Terr. Atmos. Ocean. Sci., 27, 303-309, doi: 10.3319/TAO.2016.02.02.01(AA)

1. INTRODUCTION

Heat transfer between the ocean and atmosphere is an important coupling process in the climate system (Dong et al. 2010). One of the controlling variables in air-sea heat transfer is the difference between the surface air temperature (SAT) and sea surface temperature (SST). However, unlike the SSTs, which can be observed with high precision from both microwave and infrared radiometers, SAT observations have proven difficult in space and time (Dong et al. 2010). The infrared sounder on board the Aqua satellite (Atmospheric Infrared Sounder, AIRS) is a useful tool to estimate the SAT measurements, it is however sensitive to the presence of clouds.

Global Positioning System (GPS) radio occultation (RO) is a space-borne remote sensing technique that can provide accurate, all-weather, high vertical resolution profiles of atmospheric parameters over both land and ocean (Melbourne et al. 1994). Meteorological parameters such as pressure, temperature and humidity can be derived from GPS RO observations via the fundamental retrieved bending angle of the ray and the refractivity of air (Kuo et al. 2000). Previous studies have suggested that the RO is able to provide temperature profiles with an accuracy of 1°C and less in the troposphere and stratosphere (Kursinski et al. 1997). Therefore, the GPS RO observations also provide an effective opportunity to estimate the SAT over the ocean.

SAT measurements over the Tropical Oceans were extracted from GPS RO observation in 2008 via the atmospheric temperature lapse rate, which is defined as the rate at which atmospheric temperature decreases with the increase in altitude. The Tropical Oceans (10°S - 10°N, see Fig. 1) were selected as the region of interest due to the dense in situ measurements from moored buoys in these areas, which can be used to assess SAT performance from RO observations.

2. DATA AND METHOD

The GPS RO observations from the Constellation Observing System for Meteorology Ionosphere and Climate (COSMIC)/Formosa Satellite 3 (FORMOSAT-3) were used to extract the SAT measurements in this study. The COSMIC/

* *Corresponding author*
E-mail: gpgao@shou.edu.cn

FORMOSAT-3, launched in April 2006 is a joint US/Taiwan GPS RO mission consisting of six identical micro-satellites. The COSMIC post processed level-2 wetPrf product with the newest version of 2013.3520 during 2008 is collected from the Taiwan Analysis Center for COSMIC (TACC, http://tacc.cwb.gov.tw) for further analysis. Each wetPrf file contains an atmospheric profile of altitude, pressure, latitude, longitude, refractivity, temperature, and water vapour. To obtain the 2-m SAT for air-sea heat transfer calculation the atmospheric temperature lapse rate is adopted to convert the air temperature at the lowest altitude recorded in RO product to 2-m. A typical tropical boundary layer lapse rate of 9.8°C km^{-1} is used in this study (Gosnell et al. 1995). In addition, larger errors may be introduced during the temperature conversions for the three cases listed below, which needed to be eliminated during the temperature conversions. (1) When the lowest RO profile altitude is larger than 0.5 km, where the negative bias (N-bias) in RO profiles may reach a maximum (Xie et al. 2010) and the temperature lapse rate could stray from 9.8°C km^{-1}. (2) For the low level cases temperature inversion is found in the RO profiles with altitude less than 0.5 km the low level air temperature will not obey the temperature lapse rate law. (3) Given that the number of levels in a standard RO profile is 399 (0.1 - 40 km), the RO profile levels less than 100 are excluded for SAT conversions.

European Centre for Medium-Range Weather Forecasts (ECMWF) Interim Reanalysis (ERA-Interim; Dee et al. 2011) is the third generation and latest global atmospheric reanalysis, which uses a much improved atmospheric model and assimilation system from those used in ERA-40. ERA-Interim (http://apps.ecmwf.int/datasets/data/interim_full_daily/) represents a major undertaking by ECMWF (European Centre for Medium-Range Weather Forecasts) with several of the inaccuracies exhibited by ERA-40 being eliminated or significantly reduced. In this study 2-m SAT from ERA-Interim Reanalysis at full resolution (i.e., 0.75° × 0.75° grids) every six hours (i.e., 00, 06, 12, and 18 UTC) was adopted for COSMIC derived SAT comparison and analyses.

The National Centers for Environmental Prediction Department of Energy (NCEP-DOE) Reanalysis II (designated as NCEP-II) is an improved version of NCEP Reanalysis I, which is available from 1979 to present (Kanamitsu et al. 2002). The 6-hourly NCEP-II products of 2-m air temperature, surface pressure, specific humidity, SST, and wind are interpolated in space and time to collocate with the RO measurements. The 2-m air temperature from NCEP-II is used to validate the RO derived SAT (SAT_{RO}), while the other parameters are combined with SAT_{RO} to calculate the latent (LHF) and sensible heat fluxes (SHF; namely derived LHF_{RO} and SHF_{RO} in this study) with the Coupled Ocean-Atmospheric Response Experiment bulk flux algorithm 3.0 version (COARE; Fairall et al. 2003). In addition, turbulent heat fluxes are also extracted directly from the 6-hourly NCEP-II product for comparison with our estimates.

The surface turbulent heat fluxes are also available from various other products. Objectively analyzed air-sea heat fluxes (OAFlux; Yu and Weller 2007) are constructed by integrating an optimal blending of satellite retrievals and three atmospheric reanalysis. Daily OAFlux products are available on a 1° grid for the period 1985-present. Turbulent heat fluxes from the Japanese Ocean Flux data sets with Use of Remote sensing Observations version 2 (J-OFURO2) offers global ocean fields of LHF and SHF on a 1° spatial resolution from 1988 to 2008 (Tomita and Kubota 2006). The Hamburg ocean atmosphere parameters and fluxes from satellite data version 3.2 (HOAPS-3.2) provide turbulent heat fluxes with a 1° spatial grid and 6-hourly temporal resolution covering the period from July 1987 to 2008 (Fennig et al. 2012). Similar to the NCEP-II product the turbulent heat fluxes from these three products are interpolated in the spatial and temporal domain to compare with those derived using RO observations.

The Tropical Ocean Global Atmosphere program (TOGA) is a component of the World Climate Research Programme (WCRP) that aims to predict climate phenomena on time scales of months to years (http://www.pmel.noaa.gov/tao). It includes the Tropical Atmosphere Ocean

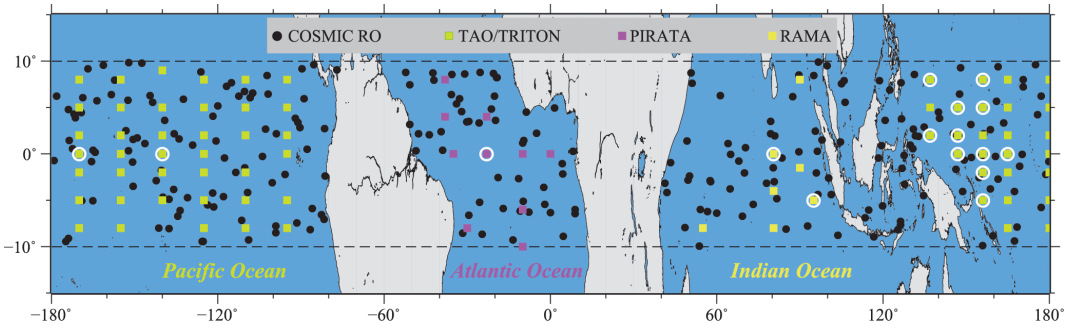

Fig. 1. Location of the region of interest. The green, purple, and yellow solid squares represent the moored buoys from the TAO/TRITON, PIRATA, and RAMA arrays, respectively. Black solid circles show an example of COSMIC RO distributions on 25 January 2008, and white hollow circles are the selected moored buoys used for assessment. (Color online only)

(TAO)/Triangle Trans-Ocean Buoy Network (TRITON) array in the Pacific, the Prediction and Research Moored Array in the Atlantic (PIRATA), and the Research Moored Array for African-Asian-Australian Monsoon Analysis and Prediction (RAMA) in the Indian Ocean. High resolution SATs from TAO/TRITON, PIRATA and RAMA were used in this study to validate SAT_{RO}. Moreover, the LHF and SHF were also estimated from TOGA observations with COARE 3.0 algorithm.

3. VALIDATION OF GPS RO DERIVED SAT IN TROPICAL OCEANS

Two criteria are applied to collect the matchup pairs from GPS RO profiles and TOGA buoys observations. First the collocation requires the distance between the GPS RO and TOGA observations to be no greater than 100 km. Second the SATs from the spatially-collocated TOGA buoy (hereafter SAT_{TOGA}) are interpolated to the SAT_{RO} observational time with spline interpolation. As a result 394 matchups were extracted in Tropical Oceans during 2008.

A scatterplot of SAT_{RO} against SAT_{TOGA} is shown in Fig. 2a. It can be seen in Fig. 2a that the SAT_{RO} agrees well with SAT_{TOGA}, with a correlation coefficient (C.C.) of 0.76, a standard deviation (STD) of 0.86°C and a root mean square (RMS) of 1.0°C, respectively. One of the possible factors contributing to the differences between SAT_{RO} from SAT_{TOGA} may be the errors introduced by the temperature lapse rate (9.8°C km^{-1}) used in this study. The large distance between the two measurements could also result in their differences. It is verified that although the STD and RMS measurements decreased slowly until the collocation distance criteria was reduced to 25 km, further improvements are observed for distances less than 25 km (see Table 1). As the collocation distance criteria is reduced to 20 km the correlation between SAT_{RO} from SAT_{TOGA} increases to 0.93, and the STD and

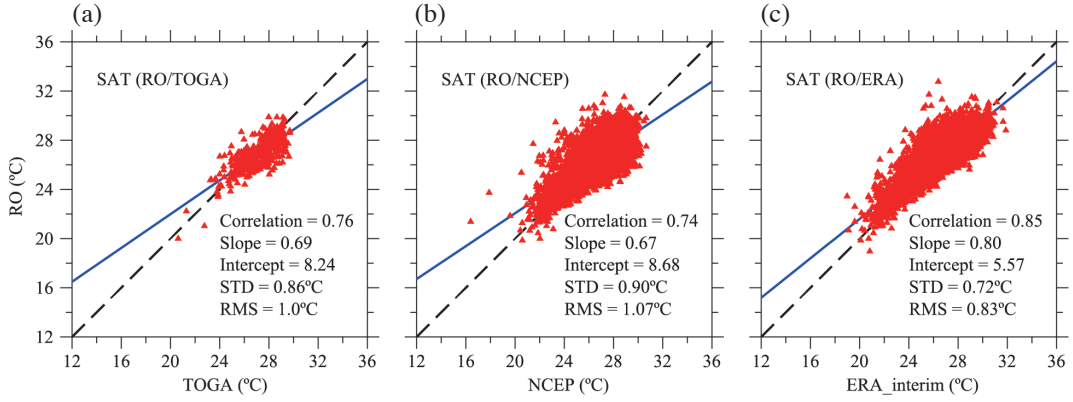

Fig. 2. Scatterplots of SAT_{RO} against (a) SAT_{TOGA}, (b) SAT_{NCEP}, and (c) SAT_{ERA}. The black dashed lines are the zero-bias line. The blue lines are the SAT_{RO} to SAT_{TOGA}, SAT_{NCEP}, and SAT_{NCEP} linear regressions, respectively. (Color online only)

Table 1. The number of matchups and linear regression results with different distances between RO and TOGA observations.

Distance (km)	Number of matchups	C.C.	STD (°C)	RMS (°C)
100	394	0.76	0.86	1.00
90	315	0.75	0.88	1.02
80	255	0.76	0.87	1.01
70	205	0.76	0.84	1.00
60	158	0.74	0.79	0.99
55	134	0.76	0.80	0.99
50	111	0.77	0.79	0.95
45	88	0.79	0.80	0.96
40	67	0.78	0.82	0.97
30	45	0.78	0.83	0.98
25	28	0.90	0.65	0.66
20	17	0.93	0.49	0.61

RMS decrease to 0.5 and 0.6°C, respectively.

For comparing the SATs from the GPS RO with the NCEP-II and ERA-Interim data (hereafter SAT_{NCEP} and SAT_{ERA}, respectively), the RO observation distance from NCEP-II and ERA-Interim data is also limited within 100 km. In addition, considering the ERA-Interim grid spatial resolution is less than 100 km, the matchups are collected between RO observations and the nearest ERA-Interim grid within 100 km. Both SAT_{NCEP} and SAT_{ERA} are interpolated in the temporal domain to the time of each GPS RO event. As a result 13172 and 19831 total pairs of SAT_{RO} and matched SAT_{NCEP} and SAT_{ERA} were extracted, respectively. The SAT_{RO} against SAT_{NCEP} and SAT_{ERA} scatterplots are shown in Figs. 2b and c, respectively. The agreement between SAT_{RO} and SAT_{NCEP} is similar to that in Fig. 2a, while relatively lower correlation and smaller regression slopes are obtained between SAT_{RO} and SAT_{NCEP}, as well as slightly worse STD and RMS for the differences observed between SAT_{RO} and SAT_{NCEP} (i.e., 0.90 and 1.07°C, respectively). In Fig. 2c, comparison between SAT_{RO} and SAT_{ERA} show the best agreement compared with Figs. 2a and b, which further demonstrates the effectiveness of GPS RO observations. The differences in SAT_{RO} from SAT_{NCEP} and SAT_{ERA} may result from their spatial and temporal mismatch, as well as the systemic errors for SAT_{RO} (i.e., the well-known systematic N-bias in RO derived refractivity profiles), SAT_{NCEP} and SAT_{ERA} measurements.

In order to understand the uncertainty in the temperature lapse rate in SAT_{RO} estimation, SAT_{RO} comparisons with SAT_{TOGA}, SAT_{NCEP}, and SAT_{ERA} with different temperature lapse rates from 5.8 - 10.8°C km^{-1} were analyzed, as shown in Table 2. As we can see in Table 2 the correlation coefficient and STD performances are stable with different temperature lapse rates during comparisons with the above three datasets. An obvious discrepancy in the RMS difference is observed when different temperature lapse rates are selected. However, a STD of less than 0.9°C and a RMS of less than 1.1°C were achieved for SAT_{RO} with the selected temperature lapse rate in this study (i.e., 9.8°C km^{-1}), indicating our choice of temperature lapse rate is reasonable. Therefore, the derived SAT_{RO} is further incorporated for turbulent heat fluxes estimation in the next section.

4. COMPARISONS AMONG TURBULENT HEAT FLUXES FROM RO OBSERVATIONS, GRIDDED HEAT FLUXES PRODUCTS AND TOGA MEASUREMENTS

To investigate whether the SAT_{RO} are accurate enough to estimate turbulent heat fluxes the SAT_{RO} is incorporated into the COARE 3.0 algorithm to derive the LHF and SHF in this section. All other input parameters (i.e., downward solar irradiance, down welling long wave irradiance, wind speed, SST, specific humidity, and surface air pressure) required for COARE 3.0 are extracted from NCEP-II data. Other available gridded heat flux products from NCEP-II (LHF_{NCEP}, SHF_{NCEP}), OAFlux (LHF_{OA}, SHF_{OA}), J-OFURO2 (LHF_{JO}, SHF_{JO}), and HOAPS-3.2 (LHF_{HO}, SHF_{HO}) are used for comparison. As mentioned above, turbulent heat flux comparisons were also performed within the 100 km distance.

The overall turbulent heat flux comparisons from RO against those from NCEP-II, OAFlux, J-OFURO2, and HOAPS-3.2 are given in Fig. 3. Heat fluxes out of the ocean are defined as positive. RO derived LHF (LHF_{RO}) comparison with LHF_{NCEP} in Fig. 3a shows a correlation of 0.95 and a STD of 13.5 W m^{-2}, respectively, but it experiences an unsatisfactory RMS of 50.8 W m^{-2}. Despite the correlation (0.61) and STD (32.1 W m^{-2}) between LHF_{RO} and LHF_{OA} (Fig. 3b) performance being worse than that in Fig. 3a, the coincidence comparison in Fig. 3b experiences a smaller RMS of 42.3 W m^{-2}. In addition, the regression analysis between LHF_{RO} and LHF_{OA} gives a slope closest to the zero-bias line, suggesting that the LHF_{RO} can capture the full range of LHF_{NCEP} values. Moreover, a correlation of 0.49, a STD of 34.9 W m^{-2}, and a RMS of 47 W m^{-2} between LHF_{RO} and LHF_{JO} are observed in Fig. 3c, respectively. As can be seen from Fig. 3d, the LHF_{RO} and LHF_{HO} comparison performs worst since the lowest correlation and slope of 0.42 and 0.28 are observed, together with the largest STD and RMS of 37.2 and 65.4 W m^{-2}, respectively.

In Fig. 3e, unlike the high correlation (0.95) between LHF_{RO} and LHF_{NCEP} in Fig. 3a, the correlation between SHF_{RO} and SHF_{NCEP} is found to be only 0.42. As described above the main difference between RO and NCEP-II derived turbulent heat fluxes lies in the fact that different SAT measurements are used during COARE 3.0 algorithm implementation, while the other meteorological parameters are all extracted from NCEP-II data. It can therefore be concluded that the SHF is more sensitive to the SAT errors than LHF. Additionally, SHF_{RO} and SHF_{OA} comparison in Fig. 3f shows a correlation of 0.46, a STD of 7.75 W m^{-2} and a RMS of 9.33 W m^{-2}, indicating that SHF_{RO} performance is better when compared with SHF_{OA} than compared with SHF_{NCEP}. The SHF comparisons in Figs. 3g and h exhibit poor performance because SHF_{RO} shows weak correlations with SHF_{JO} and SHF_{HO} (i.e., only 0.14 and 0.27, respectively), as well as the regression slopes are observed to be only 0.16 and 0.28, respectively. Therefore, LHF_{RO} and SHF_{RO} show the best agreement with the OAFlux results. It is clear in Fig. 3 that the linear regression slope in each scatterplot is lower than that of the zero-bias line, which may result from the N-bias observed in Fig. 2, as well as the temporal and spatial discrepancies between the RO derived turbulent heat fluxes and above turbulent heat flux products.

Although the turbulent heat fluxes retrieved by ship and buoy observations suffer from the poor spatial resolution and high cost, they are still thought to be the most accurate way

to monitor oceanic turbulent heat fluxes. Therefore, in order to objectively assess the RO derived turbulent heat fluxes in this study, the LHF and SHF measurements derived from RO observations and gridded heat flux products are further compared with TOGA moored buoys during 2008. Only RO events within the 100 km distance from the moored buoys were selected to estimate the LHF and SHF. The turbulent heat fluxes from the other gridded products at these sites were obtained via temporal interpolations. As a result, a total of 69 pairs of measurements are matched and their positions are illustrated in Fig. 1 with the white hollow circles. It should be noted that the white circles in Fig. 1 are fewer than 69 because the matched measurements at different times may be located at the same sites.

Figure 4 shows the spatial and temporal matched LHF and SHF estimated from RO, buoy observations, NCEP-II, OAFlux, J-OFURO2, and HOAPS-3.2, respectively. In Fig. 4a, LHF_{RO} shows the best agreement with the buoy estimated LHF (LHF_{BUOY}) compared with the other measurements. The smallest RMS difference (39.2 W m^{-2}) between LHF_{RO} and LHF_{BUOY} were obtained, followed by 54.2 W m^{-2} between LHF_{OA} and LHF_{BUOY}, 57.3 W m^{-2} between LHF_{JO} and LHF_{BUOY}, 70.6 W m^{-2} between LHF_{NCEP} and LHF_{BUOY}, and 87.3 W m^{-2} between LHF_{HO} and LHF_{BUOY} (Table 3). As for the SHF comparisons in Fig. 4b, the SHF_{RO} also shows the smallest RMS difference (6.4 W m^{-2}) against the buoy estimated SHF (SHF_{BUOY}), while RMS against SHF_{NCEP}, SHF_{OA}, SHF_{JO}, and SHF_{HO} are 8.1, 8.2, 7.8, and 11.0 W m^{-2},

Table 2. SAT_{RO} performance analysis via comparisons with SAT_{TOGA}, SAT_{NCEP}, and SAT_{ERA} when different temperature lapse rates are selected.

Lapse rate (°C km^{-1})	TOGA			NCEP-II			ERA-Interim		
	C.C.	STD (°C)	RMS (°C)	C.C.	STD (°C)	RMS (°C)	C.C.	STD (°C)	RMS (°C)
5.8	0.78	0.83	1.92	0.76	0.88	1.99	0.85	0.71	1.35
6.8	0.78	0.83	1.61	0.76	0.88	1.69	0.85	0.70	1.07
7.8	0.77	0.83	1.34	0.76	0.88	1.42	0.86	0.70	0.86
8.8	0.77	0.84	1.13	0.75	0.89	1.21	0.85	0.70	0.76
9.8	0.76	0.86	1.00	0.74	0.90	1.07	0.85	0.72	0.83
10.8	0.75	0.88	1.00	0.73	0.92	1.05	0.84	0.74	1.02

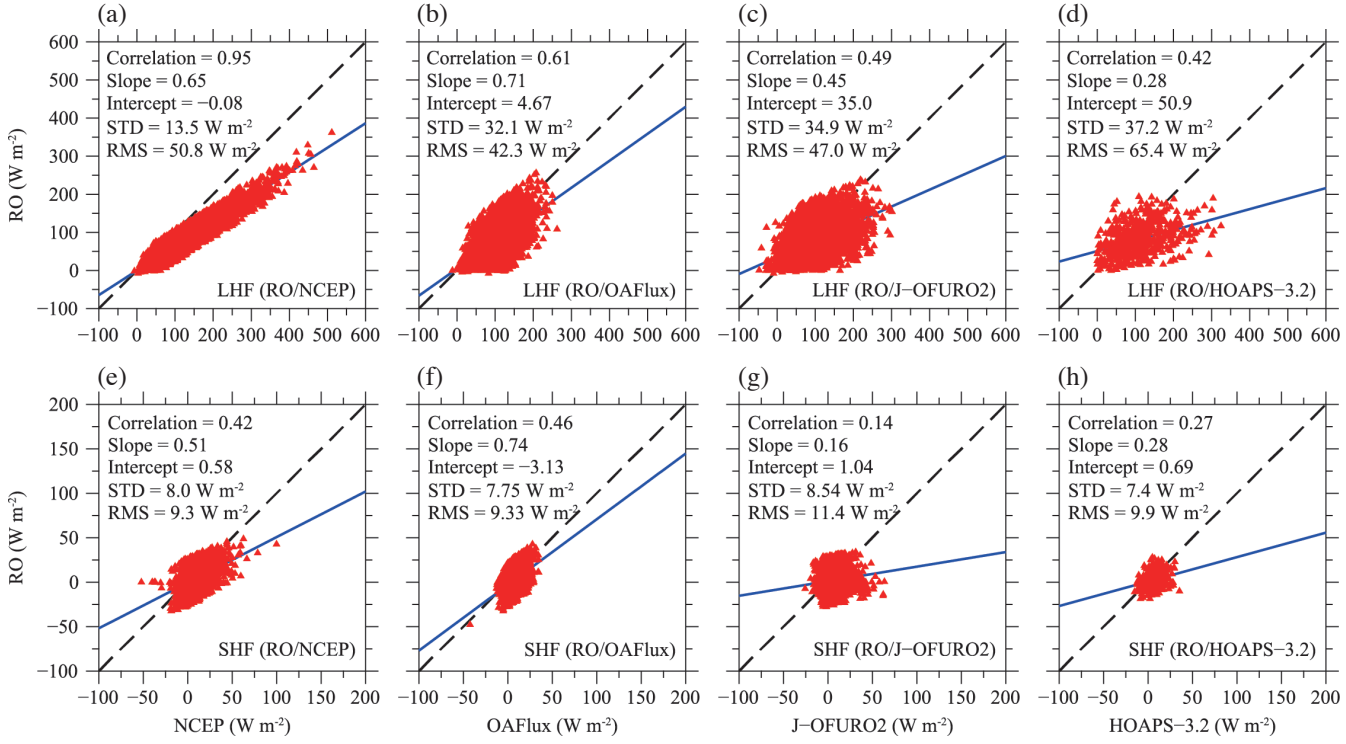

Fig. 3. Scatterplots of RO derived LHF against (a) LHF_{NCEP}, (b) LHF_{OA}, (c) LHF_{JO}, and (d) LHF_{HO}, respectively. (e) - (h) Same as (a) - (d) but for SHF. The black dashed lines are the zero-bias line. The blue lines are the linear regression. (Color online only)

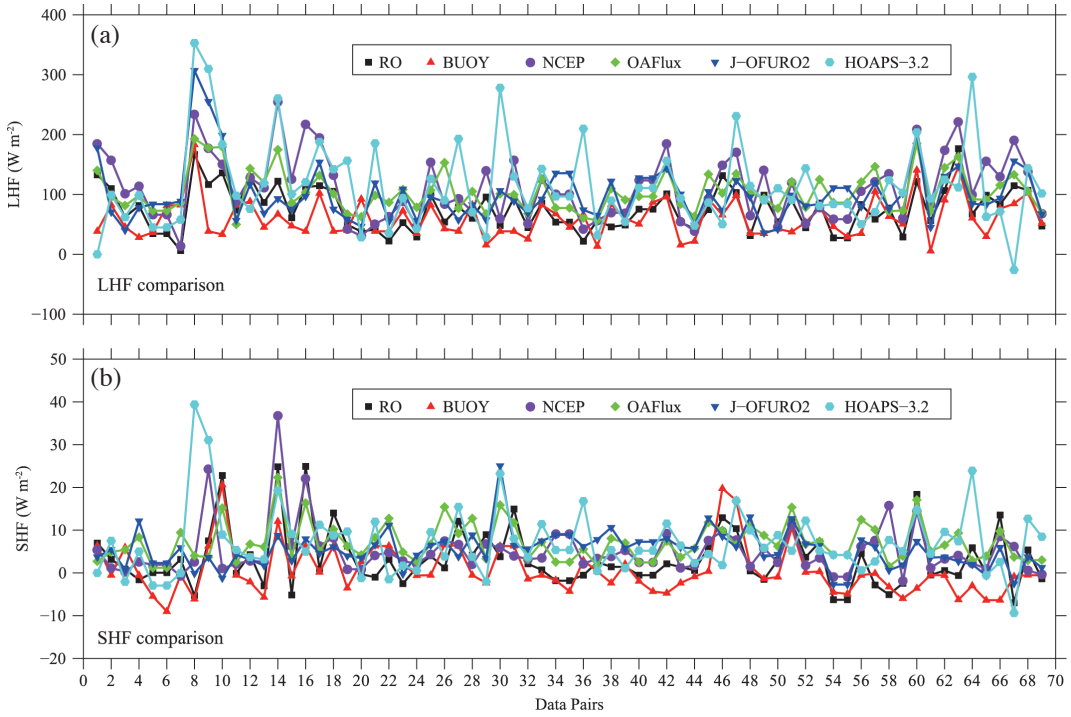

Fig. 4. (a) LHF and (b) SHF estimated from RO (black solid squares), buoy observations (red solid triangles), NCEP-II (purple solid circles), OAFlux (green solid diamonds), J-OFURO2 (blue solid inverted triangles), and HOAPS-3.2 (cyan solid hexagons) products at matched buoy sites. (Color online only)

Table 3. The RMS differences in turbulent heat fluxes from RO, NCEP-II, OAFlux, J-OFURO2, and HOAPS-3.2 against buoy measurements (Unit: W m^{-2}).

Heat fluxes	RO	NCEP-II	OAFlux	J-OFURO2	HOAPS-3.2
LHF	**39.2**	70.6	54.2	57.3	87.3
SHF	**6.4**	8.1	8.2	7.8	11.0

respectively. It can be seen from Table 3 that both the LHF and SHF measurements obtained using the HOAPS-3.2 product show the poorest performance when compared with the other measurements.

As analyzed above the turbulent heat fluxes suffer from SAT errors during COARE 3.0 bulk flux algorithm implementation. As we can see in Table 3 the RO derived turbulent heat fluxes show better performance than that from NCEP-II, despite all of the input meteorological parameters (except SAT_{RO}) for LHF_{RO} and SHF_{RO} estimation derived from NCEP-II. In other words, the SAT_{RO} measurements are helpful in improving turbulent heat flux accuracy. As such, the RO observations can also be used as supplementary measurements for SAT extraction and oceanic turbulent heat fluxes estimation.

5. CONCLUSION

This study presented a new way to estimate SATs with GPS RO observations, further incorporated to improve heat flux estimates. Our findings from this study can be summarized as follows:

(1) Comparisons of SAT_{RO} against SAT_{TOGA}, SAT_{NCEP}, and SAT_{ERA} in Tropical Oceans during 2008 show that the RMS of SAT_{RO} is better than 1.1°C and the STD is less than 0.9°C. In addition, one of the potential reasons for their difference may be the errors introduced by the temperature lapse rate used in this study. The large distance for RO observations from TOGA and NCEP-II data may also contribute to their RMS and STD differences.

(2) The overall comparisons of turbulent heat fluxes estimations from RO against those from NCEP-II, OAFlux, J-OFURO2, and HOAPS-3.2 indicate that the RO output shows the best and worst agreement with OAFlux and HOAPS-3.2, respectively. The SHF measurements are more sensitive to SAT errors than LHF.

(3) Although all of the parameters (excluding SAT_{RO}) for LHF_{RO} and SHF_{RO} estimation were adopted from

NCEP-II, the RO derived turbulent heat fluxes achieve better turbulent heat flux estimations at moored buoys in Tropical Oceans. As such, SAT_{RO} incorporation can help to improve the surface turbulent heat flux estimation.

A constant atmospheric lapse rate of 9.8°C km^{-1} was assigned in this study to derive SAT_{RO}. However, the SAT_{RO} are sensitive to the assigned atmospheric lapse rate value and the low level atmospheric condition is also not stable enough to be described by the constant lapse rate. The lowest altitude for the RO profiles maybe 0.5 km or even higher, which may also increase the errors during SAT conversions. As such, further analyses of more suitable atmospheric lapse rate can be helpful to further improve SAT_{RO} and turbulent heat flux accuracy, which would be an important issue for future research.

Acknowledgements The authors would like to thank Prof. Lung-Chih Tsai and the other Two Anonymous Reviewers for their guidance and constructive comments. This work is supported in part by the Global Change Research Program of China (2015CB953900), the National Natural Science Foundation of China (Grant Nos. 41506211 and 41276197), by the Shanghai Pujiang Program (Grant No. 12PJ1404100), by the Shanghai Sailing Program (Grant No. 14YF1410200), by the Innovation Program of Shanghai Municipal Education Commission (Grant Nos. 14YZ118 and 14ZZ148), and by the Young Teacher Training Program of Shanghai Colleges and Universities (A1-2035-15-0021-12).

REFERENCES

Dee, D. P., S. M. Uppala, A. J. Simmons, P. Berrisford, P. Poli, S. Kobayashi, U. Andrae, M. A. Balmaseda, G. Balsamo, P. Bauer, P. Bechtold, A. C. M. Beljaars, L. van de Berg, J. Bidlot, N. Bormann, C. Delsol, R. Dragani, M. Fuentes, A. J. Geer, L. Haimberger, S. B. Healy, H. Hersbach, E. V. Hólm, L. Isaksen, P. Kållberg, M. Köhler, M. Matricardi, A. P. McNally, B. M. Monge-Sanz, J. J. Morcrette, B. K. Park, C. Peubey, P. de Rosnay, C. Tavolato, J. N. Thépaut, and F. Vitart, 2011: The ERA-Interim reanalysis: Configuration and performance of the data assimilation system. *Q. J. R. Meteorol. Soc.*, **137**, 553-597, doi: 10.1002/qj.828. [Link]

Dong, S., S. T. Gille, J. Sprintall, and E. J. Fetzer, 2010: Assessing the potential of the Atmospheric Infrared Sounder (AIRS) surface temperature and specific humidity in turbulent heat flux estimates in the Southern Ocean. *J. Geophys. Res.*, **115**, C05013, doi: 10.1029/2009JC005542. [Link]

Fairall, C. W., E. F. Bradley, J. E. Hare, A. A. Grachev, and J. B. Edson, 2003: Bulk parameterization of air-sea fluxes: Updates and verification for the COARE algorithm. *J. Climate*, **16**, 571-591, doi: 10.1175/1520-0442(2003)016<0571:BPOASF>2.0.CO;2. [Link]

Fennig, K., A. Andersson, S. Bakan, C. P. Klepp, and M. Schröder, 2012: Hamburg Ocean Atmosphere Parameters and Fluxes from Satellite Data - HOAPS 3.2 - Monthly Means / 6-Hourly Composites. Satellite Application Facility on Climate Monitoring, doi: 10.5676/EUM_SAF_CM/HOAPS/V001. [Link]

Gosnell, R., C. W. Fairall, and P. J. Webster, 1995: The sensible heat of rainfall in the tropical ocean. *J. Geophys. Res.*, **100**, 18437-18442, doi: 10.1029/95JC01833. [Link]

Kanamitsu, M., W. Ebisuzaki, J. Woollen, S. K. Yang, J. J. Hnilo, M. Fiorino, and G. L. Potter, 2002: NCEP-DOE AMIP-II reanalysis (R-2). *Bull. Amer. Meteorol. Soc.*, **83**, 1631-1643, doi: 10.1175/BAMS-83-11-1631. [Link]

Kuo, Y. H., S. V. Sokolovskiy, R. A. Anthes, and F. Vandenberghe, 2000: Assimilation of GPS radio occultation data for numerical weather prediction. *Terr. Atmos. Ocean. Sci.*, **11**, 157-186.

Kursinski, E. R., G. A. Hajj, J. T. Schofield, R. P. Linfield, and K. R. Hardy, 1997: Observing Earth's atmosphere with radio occultation measurements using the Global Positioning System. *J. Geophys. Res.*, **102**, 23429-23465, doi: 10.1029/97JD01569. [Link]

Melbourne, W. G., E. S. Davis, C. B. Duncan, G. A. Hajj, K. R. Hardy, E. R. Kursinski, T. K. Meehan, L. E. Young, and T. P. Yunck, 1994: The application of spaceborne GPS to atmospheric limb sounding and global change monitoring. Technical Report, JPL-PUBL-94-18, Jet Propulsion Laboratory, United States, 158 pp.

Tomita, H. and M. Kubota, 2006: An analysis of the accuracy of Japanese Ocean Flux data sets with Use of Remote sensing Observations (J-OFURO) satellite-derived latent heat flux using moored buoy data. *J. Geophys. Res.*, **111**, C07007, doi: 10.1029/2005JC003013. [Link]

Xie, F., D. L. Wu, C. O. Ao, E. R. Kursinski, A. J. Mannucci, and S. Syndergaard, 2010: Super-refraction effects on GPS radio occultation refractivity in marine boundary layers. *Geophys. Res. Lett.*, **37**, L11805, doi: 10.1029/2010GL043299. [Link]

Yu, L. and R. A. Weller, 2007: Objectively analyzed air-sea heat fluxes for the global ice-free oceans (1981-2005). *Bull. Amer. Meteorol. Soc.*, **88**, 527-539, doi: 10.1175/BAMS-88-4-527. [Link]